Arch. Mech., **68**, 5, pp. 395–418, Warszawa 2016

Direct numerical simulation of the Taylor–Couette flow with the asymmetric end-wall boundary conditions

E. TULISZKA-SZNITKO, K. KIEŁCZEWSKI

Institute of Thermal Engineering
Poznań University of Technology
Piotrowo 3
60-965 Poznań, Poland
e-mail: ewa.tuliszka-sznitko@put.poznan.pl

In the paper the authors present the results obtained during a direct numerical simulation of the transitional Taylor–Couette flow in closed cavity. The spectral vanishing viscosity method is used to stabilize computations for higher Reynolds numbers. The Taylor–Couette flow is widely used for studying the primary pattern formation, transitional flows and fully turbulent flows. The Taylor–Couette flow is also important from engineering point of view: the results can be interesting for engineers dealing with gas turbines and axial compressors. In the paper the attention is focused on the influence of the end-wall boundary conditions on the flow structures and on statistics (i.e. the radial profiles of the angular velocity, angular momentum, torque, the Reynolds stress tensor components). The results are discussed in the light of experimental and numerical data published in literature (F. Wendt, Ing.-Arch., **4**, 1933; H. Brauckmann, B. Eckhardt, J. Fluid Mech., **718**, 2013).

Key words: Taylor–Couette flow, torque, bifurcations, direct numerical simulation, spectral vanishing viscosity method.

Copyright © 2016 by IPPT PAN

1. Introduction

In the classic Taylor–Couette system with the rotating inner cylinder and the stationary outer one the flow undergoes a series of the following subsequent transitions: Beyond a certain critical Reynolds number the circular Couette flow becomes unstable, which results in the appearance of pairs of counter-rotating axisymmetric vortices filling in the annulus. Each pair of vortices has an axial wavelength equal to dimensionless value $\lambda_z/(R_2 - R_1) = 2$. Then, a supercritical Hopf bifurcation leads to a state with waves on the vortices (in wavy vortex flow the Taylor–Couette vortical structure is retained but vortices are modified). With further increase of Re the modulated waves state and turbulent Taylor vortex flows appear. The Taylor–Couette flows are, among others, very useful from numerical and experimental points of view because of the simplicity of their geometry. These model flows provide opportunities for detailed comparisons between the experimental and numerical results. Knowledge of the local bifurcations can lead to a better understanding of the organization of more complex dynamics (global bifurcation and chaos). From application point of view these flows are particularly suitable for investigating the phenomena which occur in gas turbines, ventilations, chemical mixing equipment, in geophysics and in astrophysics.

The Taylor–Couette flow is governed by parameters defined below. The cavity is characterized by radii ratio $\eta = R_1/R_2$ (where R_1 and R_2 are the radii of the inner and outer cylinders respectively, Fig. 1), by curvature parameter $R_m = (R_2 + R_1)/(R_2 - R_1) = (1 + \eta)/(1 - \eta)$ and by aspect ratio $\Gamma = 1/L = H/(R_2 - R_1)$, where H is the axial dimension of the domain. In Figure 1 the cavity is confined by the bottom and the top end-walls. The Reynolds number is defined in the following way: $\mathrm{Re} = \Omega(R_2 - R_1)R_1/\nu$ where Ω is the rotation of the inner cylinder and the bottom disk, ν is the kinematic viscosity of the fluid.

Literature on the Taylor–Couette flow is very broad and includes experimental and numerical studies. The experimental measurements are the main source of our knowledge about the turbulent Taylor–Couette flows. Insights into the turbulent Taylor–Couette flow structure, the scaling of the torque were obtained experimentally, among others, by WENDT [1], LATHROP *et al.* [2], LEWIS, SWINNEY [3], RACINA, KIND [4]. BARCILON *et al.* [5] studied coherent structures in the turbulent Taylor–Couette flow in configuration of $\eta = 0.908$ and observed a fine herringbone-like pattern of streaks at the outer cylinder area. The review of papers in the field of the Taylor–Couette experimental research can be found in DUBRULLE *et al.* [6]. The numerical investigations, as opposed to the experimental ones, are limited to much lower Reynolds numbers. The overview of literature indicates that almost all numerical simulations, so far, have concentrated on the laminar and transitional flow cases (see MUJUMDAR, SPALDING [7], CLIFFE, MULLIN [8], CZARNY *et al.* [9], COUGHLIN, MARCUS [10, 11]). Based on the concentration of perturbations on the outflow jets boundary layers VASTANO and MOSER [12] have found that the chaos-producing mechanism leading to turbulence is a Kelvin–Helmholtz instability. DONG [13] and BRAUCKMANN, ECKHARDT [14] have recently investigated the turbulent Taylor–Couette flow by DNS (direct numerical simulation) providing detailed information on the flow structure and torque distributions.

Different configurations are considered by researchers e.g. with co- and counter-rotating cylinders, with and without an imposed axial flow and with different end-wall boundary conditions. In most numerical investigations the periodicity condition in the axial direction is applied [13, 14], which significantly reduces computational time. Such numerical results can be compared to the experimental data obtained in cavities of very large Γ. In configurations of large Γ the influence of the end-walls on a flow structure is small, but of course it exists and should be estimated. In the experimental investigations, the presence of the end-walls influences the flow structures by constraining the axial motion near the end-walls and by causing Ekman pumping. The influence of the asymmetric end-wall conditions on the flow structures in configurations of aspect ratio from the range $\Gamma = 2.4 - 3.5$, $\eta = 0.5$ (Re from 75 to 400) was studied by Mullin, Blohm [15]. They investigated numerically and experimentally the formation of the three-cell Taylor–Couette structure and its transition to the one-cell structure over the critical Re. Mullin, Blohm [15] plotted critical points of the transition as a function of Re and Γ (the general features of such bifurcations are reviewed and discussed). Theoretical analysis of the Taylor–Couette flow with the end-wall boundary conditions is beyond the scope of the present article but a lot of information the reader can find in Cliffe *et al.* [16] where the Taylor–Couette flows with the independently rotating end-walls are studied. Cliffe *et al.* [16] discussed (among others) whether the normal branch and the disconnected branch of the steady Taylor–Couette flow could be brought together in a pitchfork bifurcation at any intermediate value of the end-walls rotation rate. Problem is also investigated in Abshagen *et al.* [17]. Avila [18] performed computations for the co-rotating cylinders with the end-walls and he showed that instabilities stemming from the axial boundary conditions affect the flow globally and enhance angular momentum transport.

In [15, 16] the effect of the end-wall conditions on the bifurcations has been studied in the configurations of small aspect ratios Γ and $\eta = 0.5$ (in these flow cases the effect of the end-walls is large). In the present paper we present the results obtained for the classic Taylor–Couette flows, with the rotating inner cylinder and the stationary outer one, of aspect ratio $\Gamma = 11.75$ and radii ratio 0.9. Computations are performed for the asymmetric end-wall boundary conditions, i.e., the rotating bottom disk and the stationary top one, however, for comparison the symmetric stationary end-walls also are used. We chose the configuration of aspect ratio $\Gamma = 11.75$ because it is believed that for $\Gamma > 10$ the influence of the end-walls on the flow structure and on the statistics is negligibly small. However, our results have shown that in spite of aspect ratio greater than 10 the influence of the end-walls are still visible, particularly in the radial profiles of torque (we have tried to estimate this impact quantitatively). The radial profiles of torque we analyze in the light of the experimental data obtained by Wendt [1] and the theoretical results obtained by Eckhardt *et al* [26].

The outline of the paper is as follows. After a brief introduction (Section 1) in Section 2 we define the problem, describe the numerical method and analyze the precision of numerical computations. The flow structure, the radial profiles of the mean angular velocity and the mean angular momentum, and the Reynolds stress tensor components are presented in Section 3. The variation of torque with increasing rotation rate and the influence of the end-wall boundary conditions on it are discussed in Section 4. The conclusions are given in Section 5.

2. Mathematical and numerical approaches

We consider the incompressible flow in the Taylor–Couette cavity schematically presented in Fig. 1. The cylinder axis is aligned with the z axis of the coordinate system. The inner cylinder of radius R_1 rotates counter-clockwise (viewed toward the z direction) at a constant angular velocity Ω while the outer cylinder of radius R_2 is at rest. The top disk is stationary and the bottom one is attached to the inner rotating cylinder (for comparison the computations have also been performed for the cavity with both end-walls attached to the stationary outer cylinder).

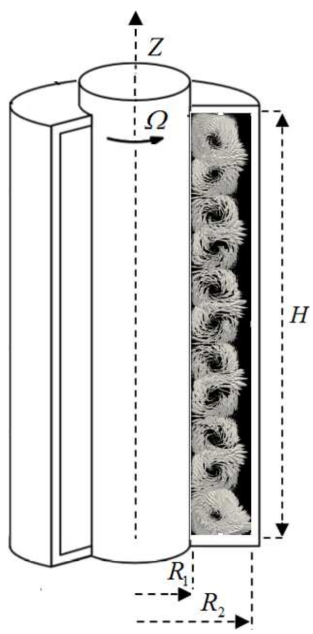

Fig. 1. Schematic picture of the Taylor–Couette flow.

The flow is described by the Navier–Stokes and continuity equations written with respect to a rotating frame of reference.

$$\nabla \cdot \mathbf{V} = 0, \tag{2.1a}$$

$$\rho \frac{\partial \mathbf{V}}{\partial \tau} + \rho(\mathbf{V} \cdot \nabla)\mathbf{V} + \rho\Omega \times (\Omega \times R) + 2\rho\Omega \times \mathbf{V} = -\nabla P + \mu \Delta \mathbf{V}, \tag{2.1b}$$

where τ is time, R is radius, P is pressure, ρ is density, $\mathbf{V}$ is the velocity vector and μ is the dynamic viscosity. The dimensionless axial and radial coordinates are: $z = Z/(H/2)$, $z \in [-1, 1]$, $r = [2R - (R_2 + R_1)]/(R_2 - R_1)$, $r \in [-1, 1]$. The dimensionless time is $t = \tau/(1/\Omega)$. The velocity components are normalized by ΩR_2; the dimensionless components of the velocity vector in radial, azimuthal and axial directions are denoted by $u = U/\Omega R_2$, $v = V/\Omega R_2$, $w = W/\Omega R_2$. No-slip boundary conditions are applied to all rigid walls $u = w = 0$. For the azimuthal velocity component, the boundary conditions are: $v = 0$ on the rotating walls and $v = -(R_m + r)/(R_m + 1)$ on the stationary walls. In order to eliminate singularities of the azimuthal velocity components at the junctions between the rotating and stationary walls, the azimuthal velocity is regularized by exponential profiles.

$$v = -1 + e^{(-z-1)/a}, \tag{2.2a}$$

$$v = -[(R_m - 1)/(R_m + 1)]e^{(z-1)/a} \tag{2.2b}$$

with $a = 0.002 - 0.005$. All presented results are obtained with the use of DNS/SVV (direct numerical simulation/spectral vanishing viscosity) method. The governing equations are approximated in time using the second-order semi-implicit scheme [19, 20, 23]. This scheme combines an implicit treatment of the diffusive term and an explicit Adams–Bashforth scheme for the non-linear convective terms. The predictor/corrector method is used. The spatial scheme is based on a pseudo-spectral Chebyshev–Fourier–Galerkin collocation approximation:

$$\Psi(r,\varphi,z) = \sum_{k=-N^\varphi/2}^{N^\varphi/2-1} \sum_{l=0}^{N^r-1} \sum_{m=0}^{N^z-1} \hat{\Psi}_{lmk} T_l(r) T_m(z) e^{ik\varphi} \qquad -1 \le r, z \le 1, \quad 0 \le \varphi \le 2\pi, \tag{2.3}$$

where $\Psi = [u^p, v^p, w^p, p^p, \phi]^T$, u^p, v^p, w^p depict predictor of the radial, azimuthal, axial velocity components, and p^p depicts the predictor of pressure, ϕ is a new variable which corrects velocity field (ϕ is described beneath in this section). In (2.3) $T_l(r)$ and $T_m(z)$ are Chebyshev polynomials of degrees l and m, respectively. N^r, N^φ and N^z are numbers of collocation points in radial, azimuthal and axial directions, respectively. In every time iteration the computations start with obtaining pressure predictor by solving Poisson equation with Neumann boundary condition. Then the velocity predictor is obtained by solving Helmholtz equation with the appropriate boundary conditions. The correction of the velocity field is done by taking into account the pressure gradient at iteration t^{i+1}, so that the final velocity field satisfies the incompressibility constraint $3(V^{i+1} - V^p)/[L(R_m+1)2\delta t] = -(\nabla p^{i+1} - \nabla p^p)$, $\nabla \cdot V^{i+1} = 0$ with the boundary condition ($V^{i+1} \cdot n = V^p \cdot n$, where δt denotes increment of time, n is normal versor). Corrected velocity components are obtained by computing new variable $\phi = 2\delta t(p^{i+1} - p^p)/3$ from the equation $\nabla\phi = \mathrm{div}(V^p)/[L(R_m + 1)]$ with the boundary condition $\nabla(\phi) \cdot n = 0$. Ultimately, the solutions of Navier–Stokes and continuity equations are obtained by solving Helmholtz equation which can be written in the following form:

$$\frac{1}{L^2}\frac{\partial^2 \Psi}{\partial r^2} + \frac{1}{L^2(R_m + r)}\frac{\partial \Psi}{\partial r} + \frac{1}{L^2(R_m + r)^2}\frac{\partial^2 \Psi}{\partial \varphi^2} + \frac{\partial^2 \Psi}{\partial z^2} - q\Psi = S, \tag{2.4a}$$

$$q = \frac{1}{L^2(R_m + r)^2} + \frac{3\mathrm{Re}}{4\delta t L^2(R_m - 1)} \qquad \text{for } v^p \text{ and } u^p, \tag{2.4b}$$

$$q = \frac{3\mathrm{Re}}{4\delta t L^2(R_m - 1)} \qquad \text{for } w^p, \tag{2.4c}$$

$$q = 0 \qquad \text{for } p^p \text{ and } \phi. \tag{2.4d}$$

Function S contains terms from the previous iterations and from the predictor stage. In next step equation (2.4a) is expanded into Fourier series; S and Ψ are described in the following way:

$$\Psi = \sum_{k=-K/2}^{K/2-1} \hat{\Psi}_k(r,z)e^{ik\varphi}, \qquad S = \sum_{k=-K/2}^{K/2-1} \hat{S}_k(r,z)e^{ik\varphi}. \tag{2.5a}$$

After expanding into Fourier series equation (2.4a) is written in the following form for each harmonic k:

$$\frac{1}{L^2}\frac{\partial^2 \hat{\Psi}_k}{\partial r^2} + \frac{1}{L^2(R_m + r)}\frac{\partial \hat{\Psi}_k}{\partial r} + \frac{\partial^2 \hat{\Psi}_k}{\partial z^2} - \left[q + \frac{k^2}{L^2(R_m + r)^2}\right]\hat{\Psi}_k = \hat{S}_k \tag{2.5b}$$

$$k \in [-N^\varphi/2, \ldots, N^\varphi/2 - 1].$$

Finally, after spatial discretization in radial and axial directions Helmholtz equation (2.4a) can be written in the following form:

$$A\Psi + \Psi B = S, \tag{2.6a}$$

$$\Psi = \hat{\Psi}_{ijk} = \hat{\Psi}_k(r_i, z_j), \qquad S = \hat{S}_{ijk} = \hat{S}_k(r_i, z_j), \qquad -1 \le r_i, z_j \le 1, \tag{2.6b}$$

where:

$$A = \frac{1}{L^2}(Dr)^{(2)}_{ij} + \frac{1}{L^2(R_m + r_i)}(Dr)^{(1)}_{ij} - \left[q_i + \frac{k^2}{L^2(R_m + r_i)^2}\right]\delta_{ij}, \tag{2.7a}$$

$$B = (Dz)^{(2)}_{ij}, \tag{2.7b}$$

$(Dr)^{(1)}_{ij}$, $(Dr)^{(2)}_{ij}$, $(Dz)^{(2)}_{ij}$ are differentiating matrices. The final system of equations is solved with full diagonalization. The described algorithm (with the energy equation) can also be used for investigation of the non-isothermal fluid flow in rotating cavity [20, 23].

To stabilize computations for higher Reynolds number we use SVV method proposed by Tadmor [21], in which an artificial viscous operator is added to Laplace operator. The Tadmor operator written in one direction has the form of

$$\tilde{\Delta}_N u_N \equiv \varepsilon_N \frac{\partial \left(Q_N \dfrac{\partial u_N}{\partial x} \right)}{\partial x},$$

where u_N is a discrete approximation of velocity component u, ε_N is the viscosity amplitude ($\lim_{N\to\infty} \varepsilon_N = 0$), Q_N is the spectral operator active only for high frequencies and N is the number of collocation points. After adding Tadmor operator (written in one direction) the Laplace operator takes the form of:

$$\nu \Delta^{SVV} u_N = \nu \Delta u_N + \varepsilon_N \frac{\partial \left(Q_N \dfrac{\partial u_N}{\partial x} \right)}{\partial x}. \tag{2.8}$$

The Tadmor operator in Fourier space is written as follows:

$$\varepsilon_N \frac{\partial \left(Q_N \dfrac{\partial u_N}{\partial x} \right)}{\partial x} = -\varepsilon_N \sum_{k_T \le |k| \le N/2} k^2 \hat{Q}_{N/2}(k) \hat{u}_k e^{ikx}. \tag{2.9}$$

In Eq. (2.9) k_T is the threshold mode above which the Tadmor [21] operator is activated. N is the number of Fourier modes. In Chebyshev space Q_N can be written in the following form:

$$Q_N \left(\frac{\partial u_N}{\partial x} \right) = \sum_{k=k_T}^{N} \hat{Q}_N(k) \left(\frac{\partial \hat{u}_N}{\partial x} \right) T_k, \tag{2.10}$$

where T_k are Chebyshev polynomials, $\hat{Q}_N(k) = 0$ for $0 \le |k| \le k_T$ and $\hat{Q}_N(k) = \exp[-[(N-|k|)/(k_T-|k|)]^2]$ for $k_T < |k| \le N$. The SVV modes are activated above assumed k_T. The 3D version of Eq. (2.8) takes the form:

$$\nu \Delta^{SVV} u_N \equiv \nu \Delta u_N + \nabla \cdot (\varepsilon_N Q_N \cdot (\nabla u_N)) = \nu (\nabla \cdot G_N \cdot \nabla) u_N, \tag{2.11}$$

where

$$\begin{aligned} G_N = I + \frac{1}{\nu}\varepsilon_N Q_N &= \begin{bmatrix} 1+\varepsilon^r_{N^r} Q^r_{N^r}/\nu & 0 & 0 \\ 0 & 1+\varepsilon^{\varphi}_{N^{\varphi}} Q^{\varphi}_{N^{\varphi}}/\nu & 0 \\ 0 & 0 & 1+\varepsilon^z_{N^z} Q^z_{N^z}/\nu \end{bmatrix} \\ &= \begin{bmatrix} G^r_{N^r} & 0 & 0 \\ 0 & G^{\varphi}_{N^{\varphi}} & 0 \\ 0 & 0 & G^z_{N^z} \end{bmatrix}. \end{aligned} \tag{2.12}$$

In Eq. (2.11) ∇u_N is the velocity gradient tensor, in Eq.(2.12) $\varepsilon^i_{N^i}$ is a viscosity amplitude for i direction and $Q^i_{N^i}$ is a viscosity operator defined in spectral space. The modified Laplace operator can be written as follows:

$$\Delta^{SVV} \equiv \frac{1}{L^2}\frac{\partial}{\partial r}G^r_{N^r}\frac{\partial}{\partial r} + \frac{1}{L^2(R_m+r)}G^r_{N^r}\frac{\partial}{\partial r} + \frac{1}{L^2(R_m+r)^2}\frac{\partial}{\partial\varphi}G^\varphi_{N^\varphi}\frac{\partial}{\partial\varphi} + \frac{\partial}{\partial z}G^z_{N^z}\frac{\partial}{\partial z}. \tag{2.13}$$

In next step Eq. (2.11) is expanded into Fourier series [22, 23, 20].

A series of calculations have been performed to validate the computational DNS/SVV approach and construct a foundation upon which further analysis can be performed with confidence. Such validation has been partly done in [23, 20]. The numerical details of the flow case $\Gamma = 11.75$, $\eta = 0.9$, $\mathrm{Re} = 2475$ are provided in Table 1. The parameters presented in Table 1 are defined in the following manner: $\Delta R_2^+ = \Delta R u_\sigma/\nu$, $\Delta R_1^+ = \Delta R u_\sigma/\nu$, where $u_\sigma = \{\nu^2[(\partial W/\partial R)^2 + (\partial V/\partial R)^2]\}^{0.25}$ is friction velocity computed at the outer and inner cylinders respectively, and $\Delta R = L(H/2)\Delta r_{\min}$; $\Delta z_2^+ = \Delta Z u_\sigma/\nu$, $\Delta z_1^+ = \Delta Z u_\sigma/\nu$, where $u_\sigma = \{\nu^2[(\partial V/\partial Z)^2 + (\partial U/\partial Z)^2]\}^{0.25}$ is friction velocity computed at the top and bottom disks respectively, and $\Delta Z = (H/2)\Delta z_{\min}$. The parameters $(R_2\Delta\varphi)^+ = R_2\Delta\varphi u_\sigma/\nu$, $(R_1\Delta\varphi)^+ = R_1\Delta\varphi u_\sigma/\nu$ are obtained for friction velocity computed at the outer and inner cylinders, and $\Delta\varphi = 2\pi/N^\varphi$. As it is shown in the Table 1 the distance of the first grid point along the wall-normal axis is smaller than one wall unit for all presented meshes. From Table 1 we can also see that compared to mesh (50, 250, 201), the radial resolution in mesh (100, 300, 201) is refined by a factor of two; this results in decreasing of $\Delta R_2^+ = \Delta R u_\sigma/\nu$ by factor four. The time step is from the range $\delta t = 0.01 - 0.0005$.

Table 1. Numerical details for the narrow-gap cavity of $\Gamma = 11.75$, $\eta = 0.9$, $\mathrm{Re} = 2475$, the results obtained for different numbers of collocation points (N^r, N^φ, N^z).

Re=2475	ΔR_2^+	ΔR_1^+	$(R_2\Delta\varphi)^+$	$(R_1\Delta\varphi)^+$	Δz_2^+	Δz_1^+
$(50, 250, 201)$	0.176	0.089	43.143	19.693	0.075	0.117
$(100, 300, 201)$	0.04349	0.02349	36.2210	17.6095	0.076	0.116
$(150, 300, 201)$	0.01905	0.01079	35.9458	18.3226	0.0768	0.116
$(100, 400, 201)$	0.04311	0.02438	26.9254	13.7079	0.076	0.116
$(100, 400, 301)$	0.04393	0.02423	27.4383	13.6234	0.034	0.0518

From the identification techniques based on pointwise analysis of the velocity gradient tensor we choose the λ_2 criterion which captures the regions of local pressure minimum [24, 25]. The iso-surfaces of λ_2 (the second, in magnitude, eigenvalue of the tensor $S_{ik}S_{kj} + \Omega_{ik}\Omega_{kj}$, where $S_{ij} = \left(\frac{\partial u_i}{\partial x_j} + \frac{\partial u_j}{\partial x_i}\right)/2$, $\Omega_{ij} = \left(\frac{\partial u_i}{\partial x_j} - \frac{\partial u_j}{\partial x_i}\right)/2$) show perfectly well the flow structure in three-dimensional space.

3. The selected result

3.1. The structure of the Taylor–Couette flow with the asymmetric end-wall boundary conditions

3.1.1. The flow case of $\Gamma = 3.76$. The purpose of this article is the investigation of the flow case of medium aspect ratio ($\Gamma = 11.75$) with the asymmetric end-wall boundary conditions, however, this investigation is a part of our wider numerical study which has been carried out, among other, in configurations of $\Gamma = 3.76$ and radii ratios $\eta = 0.375$, 0.523, 0.615, 0.756, 0.82. Those studies have shown that the influence of the end-walls depends on Γ and η. For the configuration of aspect ratio $\Gamma = 3.76$, $\eta = 0.375$ with a rotating inner cylinder and bottom disk, and with a stationary outer cylinder and top disk the three-cell structure is formed at Reynolds number $\mathrm{Re} = 77$. The odd number of vortices is a characteristic feature of the Taylor–Couette flow with the asymmetric end-wall boundary conditions. The inward flow towards the rotating inner cylinder occurs along the stationary top disk and an outward flow along the rotating bottom disk. At about $\mathrm{Re} = 270$ the middle vortex is squeezed by the growth of the vortex adjacent to the bottom rotating disk. Finally, the steady three-cell structure collapses to a one-cell state at the critical Reynolds number via a saddle-node bifurcation. We estimate this critical Re at 281. The transition to unsteadiness for cavity of aspect ratio $\Gamma = 3.76$ ($\eta = 0.375$) occurs at $\mathrm{Re} = 492$. At this Re we observe six spirals of the dimensionless azimuthal wavelength $\lambda_a/(H/2) = (2\pi R/n)/(H/2) = 0.6128$, where n is number of vortices [20]. For $\Gamma = 3.76$, $\eta = 0.375$ we observe a kind of competition between the Taylor–Couette and Batchelor flow patterns, as to which pattern will dominate the flow. The computations performed for the aspect ratio $\Gamma = 3.76$ and for different η have shown that the transition from the there-cell structure to the one-cell structure occurs for the lower η. For higher radii ratios ($\eta = 0.82$, for example) we observe the typical Taylor–Couette flow transition process. Figure 2a shows the modulated wave flow structure obtained for $\Gamma = 3.76$, $\eta = 0.82$, $\mathrm{Re} = 989$.

The behavior in time of the chosen dependent variables we monitor in the middle section of the cavity ($r = 0$) and in three different axial positions corresponding to the stationary disk layer, the geostrophic core and the rotating disk layer. The histories of the dependent variables allow us to monitor the amplitudes and angular frequency of disturbances. The exemplary history of the azimuthal velocity component obtained near the top stationary disk and in the middle sec-

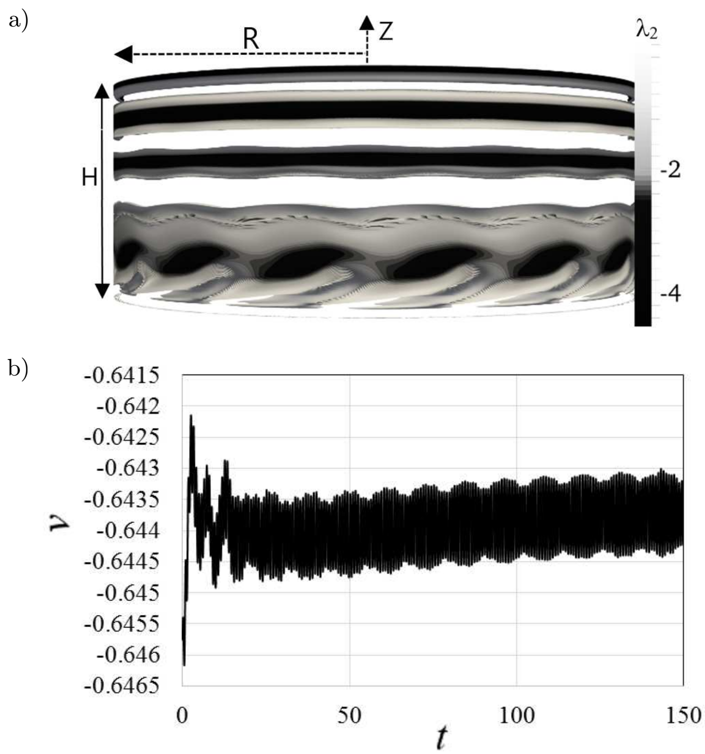

Fig. 2. a) The iso-surfaces of λ_2 obtained along the cylindrical surface near the inner cylinder, b) the azimuthal velocity component v as a function of the dimensionless time t, $\Gamma = 3.76$, $\eta = 0.82$, Re = 989, the inner cylinder and the bottom disk rotate.

tion of cavity (Fig. 2b, $\eta = 0.82$) shows that on the fundamental wave, another wave of smaller angular frequency is superimposed. For the cavity of $\Gamma = 3.76$, $\eta = 0.82$ we observe fifteen vortices coming from the Ekman boundary layer of $\lambda_a/(H/2) = 1.136$ (Fig. 2a). For this flow case we do not observe collapsing procedure, which takes place in the configuration of $\Gamma = 3.76$, $\eta = 0.375$, but we can see that the influence of the end-walls is strong. Detailed analysis of the flow cases of $\Gamma = 3.76$ with radii ratio η from 0.375 to 0.82 will be the object of a separate paper.

3.1.2. The flow case of $\Gamma = 11.75$. The study of this flow case has allowed us to analyze all the subsequent bifurcations which appear with an increasing Reynolds number for both symmetric and asymmetric end-wall boundary conditions. The Taylor–Couette vortices are formed slightly above Re = 80 which agrees well with 84 < Re < 86 obtained by Pirro, Quadrio [27] for $\eta = 0.95$, and 68.2 < Re < 68.4 obtained for $\eta = 0.5$ (in both flow cases the periodicity condi-

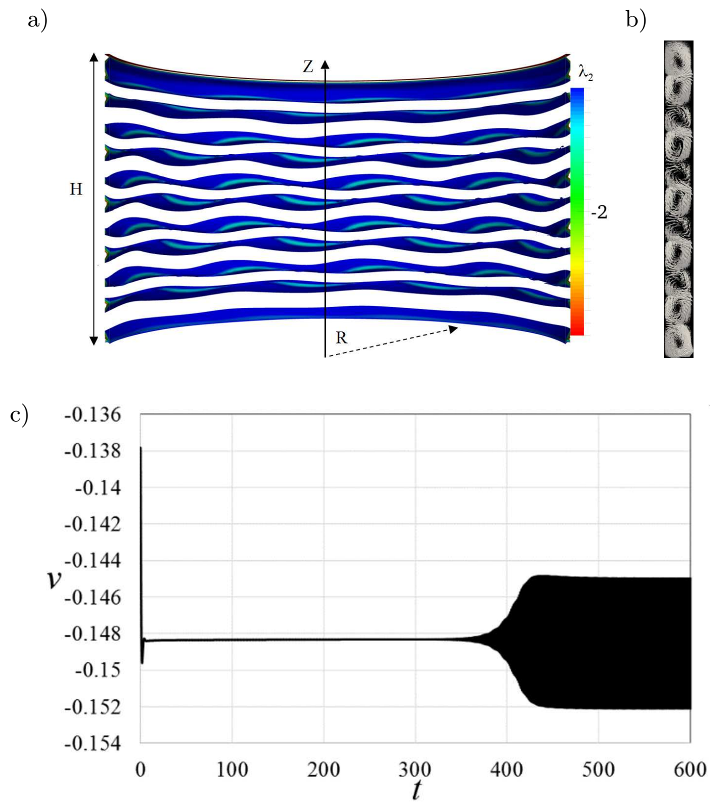

FIG. 3. a) The iso-surfaces of λ_2 obtained along the cylindrical surface near the inner cylinder, Re = 200, b) the meridian flow, Re = 200, c) the azimuthal velocity component v as a function of time, Re = 200.

tions in the axial direction have been used). Above Re = 80 we observe eleven Taylor–Couette vortices (the Taylor–Couette vortices in the meridian section are presented in Fig. 3b).

The transition to unsteadiness takes place at Re = 200 which is manifested by the appearance of wavy vortices i.e. the Taylor–Couette vortices undergo a wavy azimuthal deformation. The wave flow structure is illustrated in Fig. 3a, where we observe nine waves of $\lambda_a/(H/2) = 1.128$ propagating in the azimuthal direction. Figure 3c presents the history of the azimuthal velocity component (obtained at collocation point: $r = 0$, $z = 0.8$, $\varphi = 0$) from which we can see that the change of rotation initiates disturbance, which is then rapidly damped. After this, the flow temporarily reaches steady state that lasts up to dimensionless time $t = 350$. From $t = 350$ up to $t = 420$ we observe the exponential growth of disturbance which finally reaches an asymptotic state of the angular frequency $\sigma = 2\pi/\Delta t = 5.02$, where Δt is a period of time.

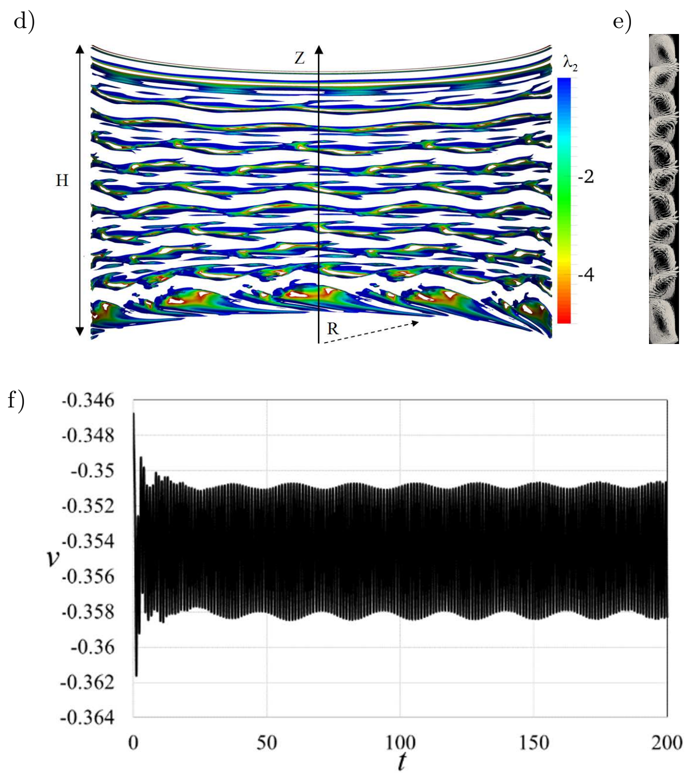

Fig. 3. [cont.] d) The iso-surfaces of λ_2 obtained along the cylindrical surface near the inner cylinder, Re = 1161, e) the meridian flow, Re = 1161, f) the azimuthal velocity component v as a function of time, Re = 1161, $\mathit{\Gamma} = 11.75$, $\eta = 0.9$, the asymmetric end-wall boundary conditions.

With further increase of Re, the bifurcation to modulated vortices appears (critical Re is estimated at 981). From the history of the azimuthal velocity component v obtained for Re = 1161 we can see that on the fundamental wave (of angular frequency $\sigma = 5.02$) the second wave of angular frequency $\sigma = 0.287$ is superimposed (Fig. 3f). With increasing Re the flow becomes gradually chaotic. The structures of the flow obtained for Re = 2475 along the cylindrical surfaces near the inner cylinder (Fig. 4a) and the outer cylinder (Fig. 4b) show the existence of many small-scale vortices extended along the azimuthal direction. However, the large-scale Taylor vortices still occupy the entire gap, with well-defined inflow and outflow jets. Nine vortices coming from the Ekman boundary layer are slightly growing in axial direction with the increasing Re, but, their influence on the entire flow is small in comparison to the flow case of $\mathit{\Gamma} = 3.76$ shown in Fig. 2.

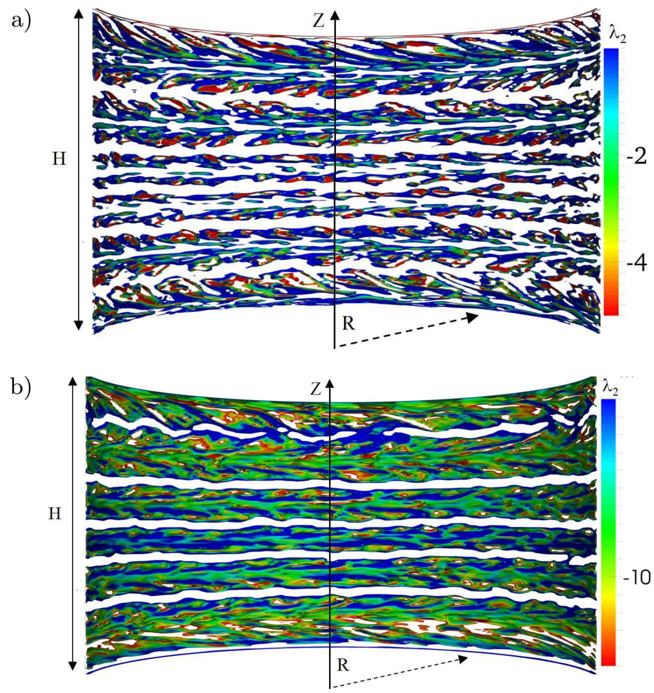

Fig. 4. The iso-surfaces of λ_2 obtained along the cylindrical surface: a) near the inner cylinder, b) near the outer cylinder, $\Gamma = 11.75$, $\eta = 0.9$, $\mathrm{Re} = 2475$, the asymmetric end-wall boundary conditions.

3.2. The radial profiles of statistical data (the flow case of $\Gamma = 11.75$)

The change in flow dynamics with increasing Re is visible in the radial profiles of angular velocity and angular momentum as it has been pointed out in [14]. The angular velocity and the angular momentum normalized by their values at the inner cylinder and averaged along cylindrical surfaces and time are presented in Fig. 5a. The averaged values are written in the following way:

$$\text{(3.1a)} \qquad \langle (V/R)/(V/R)_1 \rangle_{A(R),t} \\ = \langle [v + (R_m + r)/(R_m + 1)] \cdot [(R_m - 1)/(R_m + r)]/\eta \rangle_{A(R),t},$$

$$\text{(3.1b)} \qquad \langle (VR)/(VR)_1 \rangle_{A(R),t} \\ = \langle [v + (R_m + r)/(R_m + 1)] \cdot [(R_m + r)/(R_m - 1)]/\eta \rangle_{A(R),t},$$

where $\langle \ldots \rangle_{A(R),t}$ stands for average over a cylindrical surface of radius R and time [14]. The results presented in Fig. 5a are obtained for $\mathrm{Re} = 2025$ and $\mathrm{Re} = 2655$. We observe very narrow shear-driven boundary layers at the inner and outer cylinders. At the central part of cavity the angular velocity profiles decrease very slowly with r, while the angular momentum profiles are almost constant. This constant value is close to $(VR_1)/2$. The similar value was obtained in [14] numerically for $\eta = 0.71$ (Re = 16875), and experimentally by Taylor [28] and Smith, Townsend [29]. Figure 5b shows the comparison of the radial profile of the azimuthal velocity component (obtained for Re = 60 in the middle section of the cavity using DNS/SVV) and the theoretical solution obtained for laminar flow [27]:

$$V/\Omega R_1 = (R_1/R - \eta^2 R/R_1)/(1-\eta^2). \tag{3.2}$$

We can see an agreement between the present DNS result and the theoretical one. In contrast to turbulent flow the laminar solution constitutes almost a straight line.

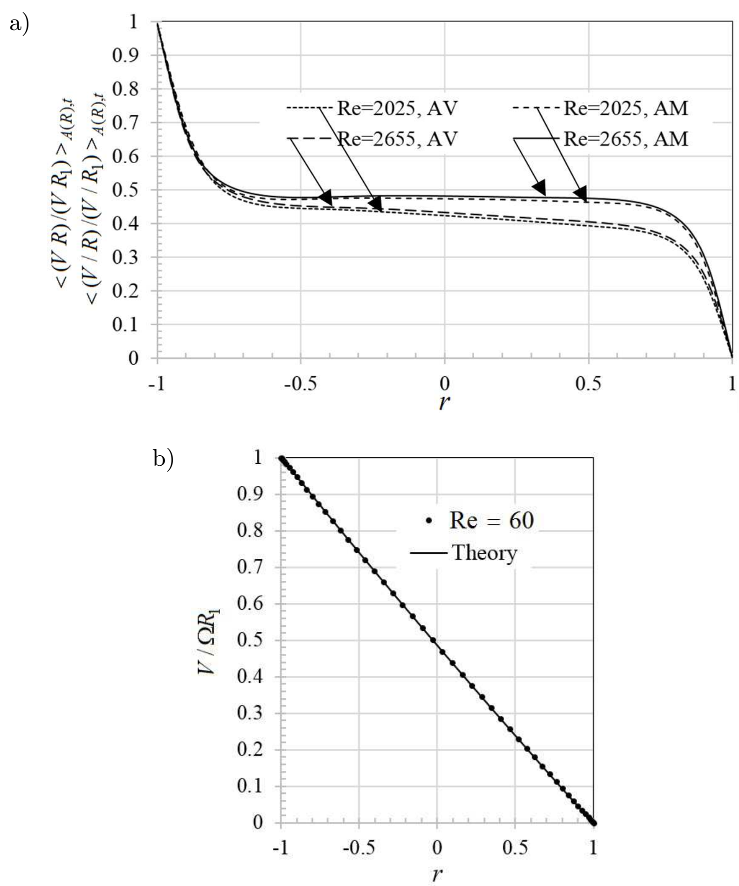

Fig. 5. a) The radial profiles of the mean angular velocity (AV) and the mean angular momentum (AM) obtained using DNS/SVV for Re = 2025 and 2655, b) the radial profile of the azimuthal velocity component obtained using DNS/SVV for Re = 60 compared with the theoretical solution, Eq. (3.2), $\Gamma = 11.75$, $\eta = 0.9$.

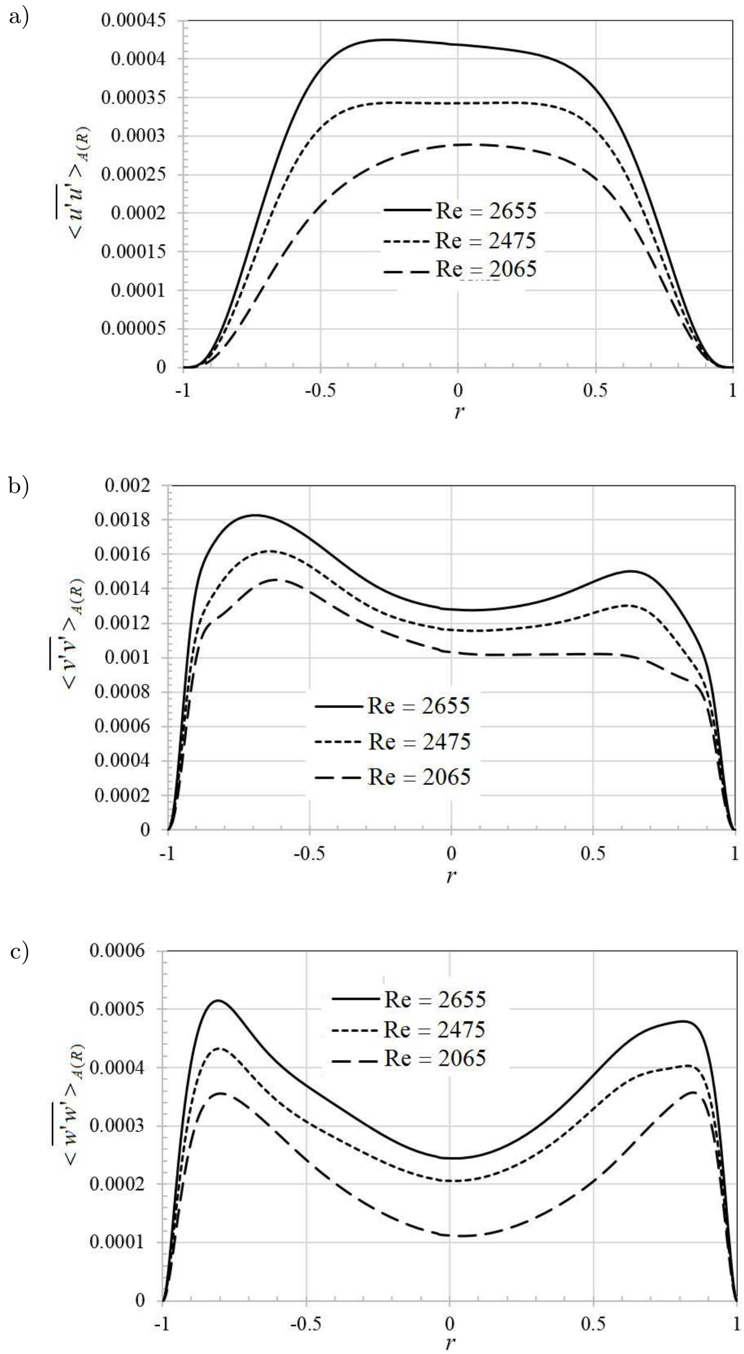

Fig. 6. The radial profiles of the Reynolds stress tensor components: a) $\langle\overline{u'u'}\rangle_{A(R)}$, b) $\langle\overline{v'v'}\rangle_{A(R)}$, c) $\langle\overline{w'w'}\rangle_{A(R)}$, $\varGamma = 11.75$, $\eta = 0.9$.

The radial profiles of the Reynolds stress tensor components averaged over a cylindrical surface are showed in Fig. 6. The results are obtained for Re = 2655, 2475 and 2065. From Fig. 6 we can see that the level of fluctuations increases with increasing Re. The highest levels of fluctuations are observed within the boundary layers for the azimuthal component (Fig. 6b). Those radial profiles show asymmetry (Fig. 6b). The profiles of the axial components are more symmetric than azimuthal ones (Fig. 6c). The profiles of radial components differ from the others, i.e., the profiles have the highest values in the middle part of cavity (Fig. 6a).

4. Variation of torque with increasing Reynolds number (the flow case of $\varGamma = 11.75$)

In the Taylor–Couette system intensive molecular and convective transfer of azimuthal momentum takes place. The azimuthal momentum needed to drive the cylinder can be measured as a torque. This issue was discussed among other by Lathrop *et al.* [2] and Lewis, Swinney [3]. The dependence of torque on the Reynolds number is of great interest for understanding the global features of the flow. The dimensionless torque is defined in the following manner $G = T/(2\pi H\rho\nu^2)$, where ρ is the density of the fluid, ν is the kinematic viscosity and H is the length of the cylinders. The main object of interest is the relation between the dimensionless torque G and Reynolds number described as follows: $G \propto \mathrm{Re}^{\alpha}$, where α is a scaling exponent. The value of α depends on Re and ranges from 1.6 to 1.8 for $\mathrm{Re} = 10^4$–10^6. Wendt [1] proposed value $\alpha = 1.5$ for $\mathrm{Re} = 4 \cdot 10^2$–$10^4$ and $\alpha = 1.7$ for $\mathrm{Re} = 10^4$–10^5. Eckhardt *et al.* [26] and Brauckmann, Eckhardt [14] performed theoretical and numerical investigations of the turbulent Taylor–Couette flows in the infinitely long cavity. In [14, 26] the torque is studied via the transverse current

$$j^{\omega} = R^3\left[\frac{UV}{R} - \nu\frac{\partial\left(\frac{V}{R}\right)}{\partial R}\right]$$

which measures the transport of angular momentum. Eckhardt *et al.* [26] showed theoretically that the mean current

$$\begin{aligned}(4.1)\qquad J^{\omega} &= \langle j^{\omega}(R,\varphi,Z,t)\rangle_{A(R),\tau} = \left\langle R^3\left[\frac{UV}{R} - \nu\frac{\partial\left(\frac{V}{R}\right)}{\partial R}\right]\right\rangle_{A(R),\tau} \\ &= R^3\left[\left\langle\frac{UV}{R}\right\rangle_{A(R),\tau} - \nu\frac{\partial\left\langle\left(\frac{V}{R}\right)\right\rangle_{A(R),\tau}}{\partial R}\right]\end{aligned}$$

is independent of radius. The mean current is related to the dimensionless torque in the following way $G = T/(2\pi H\rho\nu^2) = J^\omega/\nu^2$. By analogy to the Nusselt number (describing the heat flux in thermal convection) the mean current is often normalized by its laminar value $\mathrm{Nu}^\omega = J^\omega/J^\omega_{lam} = G/G_{lam}$, where J^ω_{lam} is the value obtained for the circular Couette flow

$$J^\omega_{lam} = \frac{2\nu R_1^2 R_2^2 V_1}{[R_1(R_2^2 - R_1^2)]}.$$

We have employed an azimuthal average in addition to the temporal one and define the turbulent velocity $U = \bar{U} + U'$ with the mean velocity $\overline{U} = \langle U\rangle_{\varphi,\tau}$. The velocity decomposition to the turbulent velocity and the mean velocity ($\overline{U'V'} = \overline{UV} - \bar{U}\,\bar{V}$) allows to analyze the contribution of the turbulent term $R^3\langle\frac{\overline{U'V'}}{R}\rangle_{A(R)}$, the mean convection term $R^3\langle\frac{\bar{U}\,\bar{V}}{R}\rangle_{A(R)}$ and the viscous term $-\nu\frac{\partial\langle\frac{\bar{V}}{R}\rangle_{A(R)}}{\partial R}$ to the total value. Values with crossbar at the top are obtained by averaging in time. After decomposition and normalization the equation (4.1) can be written in the following form, [14]:

$$\begin{aligned}\mathrm{Nu}^\omega &= R^3\left[\left\langle\frac{UV}{R}\right\rangle_{A(R),\tau} - \nu\frac{\partial\left\langle\left(\frac{V}{R}\right)\right\rangle_{A(R),\tau}}{\partial R}\right]/J^\omega_{lam}\\ &= R^3\left\langle\frac{\bar{U}\bar{V}}{R}\right\rangle_{A(R)}/J^\omega_{lam} + R^3\left\langle\frac{\overline{U'V'}}{R}\right\rangle_{A(R)}/J^\omega_{lam}\\ &\quad - \nu\frac{\partial\left\langle\left(\frac{\bar{V}}{R}\right)\right\rangle_{A(R)}}{\partial R}/J^\omega_{lam}.\end{aligned} \tag{4.2}$$

The following terms

$$\left\langle\frac{U'\bar{V}}{R}\right\rangle_{A(R),\tau}, \quad \left\langle\frac{\bar{U}V'}{R}\right\rangle_{A(R),\tau}, \quad \frac{\partial\langle\left(\frac{V'}{R}\right)\rangle_{A(R),\tau}}{\partial R}$$

are zero by definition. Following [14], in Fig. 7 we analyze contributions of the mean convective term, the turbulent term and the viscous term to Nu^ω ($\mathrm{Re} = 2475$). The largest contribution to the total current in the central part derives from the mean convective term (this term vanishes near the cylinders). The contribution of the turbulent term in considered range of Re is small. The viscous term dominates near the cylinders, which results from the shape of the angular velocity profile presented in Fig. 5a (almost flat profile in the central region with large gradients at the boundaries).

Figures 8a and 8b present the radial profiles of Nu^ω obtained for different Re, and for the asymmetric and symmetric end-wall boundary conditions, respectively. All profiles indicate a slight dependence on r. We also observe that

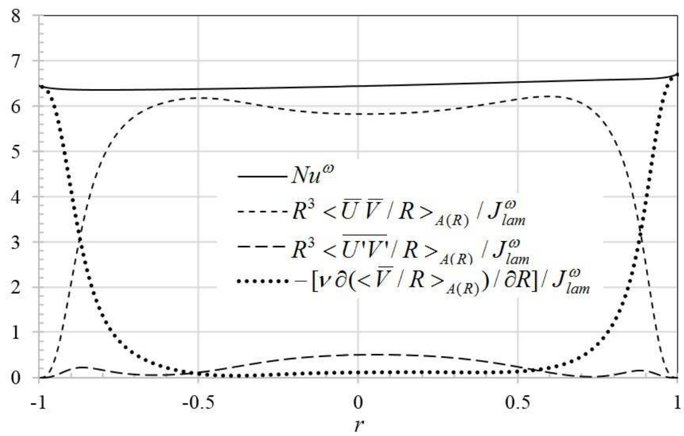

Fig. 7. The radial profiles of contributions to Nu^ω obtained for $\mathrm{Re} = 2475$, $\Gamma = 11.75$, $\eta = 0.9$.

the maximum of Nu^ω occurs at the outer cylinder ($r = 1$) in the flow cases with the asymmetric end-wall conditions and at the inner cylinder for the symmetric conditions ($r = -1$) (Fig. 8). The differences result from the different flow structures and also from location of singularities between the rotating and stationary walls. In the flow cases with the asymmetric end-walls the singularities of the azimuthal velocity component occur at the junction between the rotating bottom disk and the stationary outer cylinder, and at the junction between the stationary top disk and the rotating inner cylinder. In the flow cases with the symmetric end-walls the singularities of the azimuthal velocity component occur at the junction between the stationary bottom and top disks, and the rotating inner cylinder.

In Fig. 8c we analyze the value of $(\mathrm{Nu}_2^\omega - \mathrm{Nu}_1^\omega)/\mathrm{Nu}_1^\omega$ as a function of Re. The results presented in Fig. 8c are obtained for the flow cases with the asymmetric end-wall boundary conditions using the mesh $N^r = 100$, $N^\varphi = 300$, $N^z = 201$ (for $\mathrm{Re} = 2475$ the results obtained for the meshes of (100, 400, 201), (150, 300, 201) and (50, 250, 201) are also presented for comparison). From Fig. 8c we can see that the difference $(\mathrm{Nu}_2^\omega - \mathrm{Nu}_1^\omega)/\mathrm{Nu}_1^\omega$ takes values from the range 0.03–0.042.

The total torque Nu^ω is obtained as the spatial average over a local quantity. The fluctuations of the local quantity are influenced by flow-structures and show different characteristics near the cylindrical walls and in the middle of the cavity. This is visible in Fig. 9b, 9c and 9d, where the axial profiles of the local current averaged in time and in azimuthal direction, and normalized by J^ω_{lam} ($\langle j^\omega \rangle_{\varphi,t}/J^\omega_{lam}$), are presented (the horizontal scaling is not identical to increase readability of the results). The extreme values are observed in the middle section, where values are about 20 times larger than these along the inner and outer

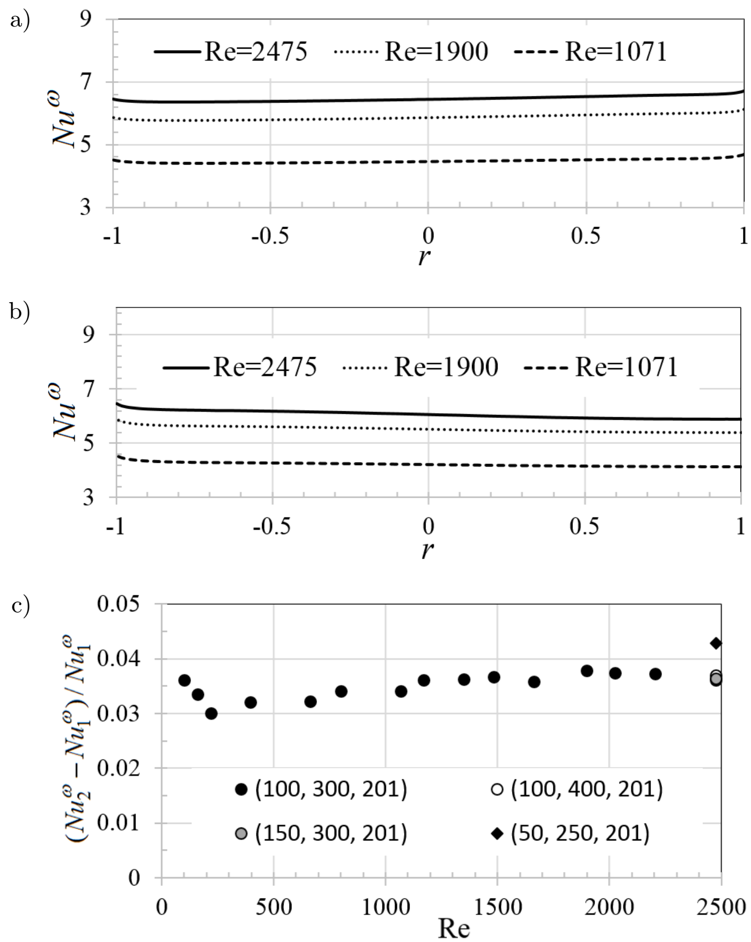

FIG. 8. The radial profiles of Nu^{ω} obtained for different Re, and for: a) the asymmetric end-wall boundary conditions (the bottom disk and inner cylinder rotate), b) the symmetric end-wall boundary conditions (the inner cylinder rotates), c) $(\mathrm{Nu}_2^{\omega} - \mathrm{Nu}_1^{\omega})/\mathrm{Nu}_1^{\omega}$ as a function of Re, the asymmetric end-wall boundary conditions, $\Gamma = 11.75$, $\eta = 0.9$.

cylinders. Despite of these large fluctuations, the averaged values over z direction are equaled to these presented in Fig. 8. The local peaks are observed at a junction between the rotating bottom disk and the stationary outer cylinder ($r = 1$, $z = -1$, Fig. 9b), and between the stationary top disk and the rotating inner cylinder ($r = -1$, $z = 1$, Fig. 9d). The comparison of Fig. 9a, where the meridian flow is displayed, with Fig. 9b, 9c and 9d shows that the local extreme values of $\langle j^{\omega}\rangle_{\varphi,t}/J^{\omega}_{lam}$ are connected with the inflow and outflow jets. At the locations of the outflow jets we observe the maximum values of $\langle j^{\omega}\rangle_{\varphi,t}/J^{\omega}_{lam}$ at the outer cylinder and in the middle section, and the minimum at the inner cylinder. At the locations of the inflow jets we observe minimum values at the

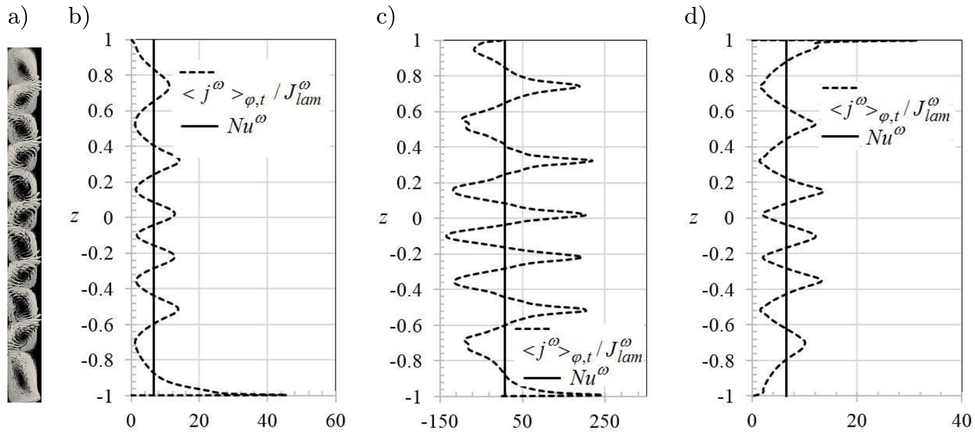

Fig. 9. a) The meridian flow structure. The axial profiles of the local current averaged in time and in azimuthal direction, and normalized by J^{ω}_{lam} along: b) the outer cylinder, c) in the middle section, d) along the inner cylinder. The comparison of $\langle j^{\omega}\rangle_{\varphi,t}/J^{\omega}_{lam}$ with the Nu^{ω}. The asymmetric end-wall boundary conditions (the bottom disk and inner cylinder rotate), $\Gamma = 11.75$, $\eta = 0.9$, $\mathrm{Re} = 2475$.

outer cylinder and in the middle section (negative), and the maximum values at the inner cylinder.

Eckhardt *et al.* [26, 30] investigated theoretically the dependence of Nu^{ω} on radii ratio η and on Reynolds number (they also interpreted measurements

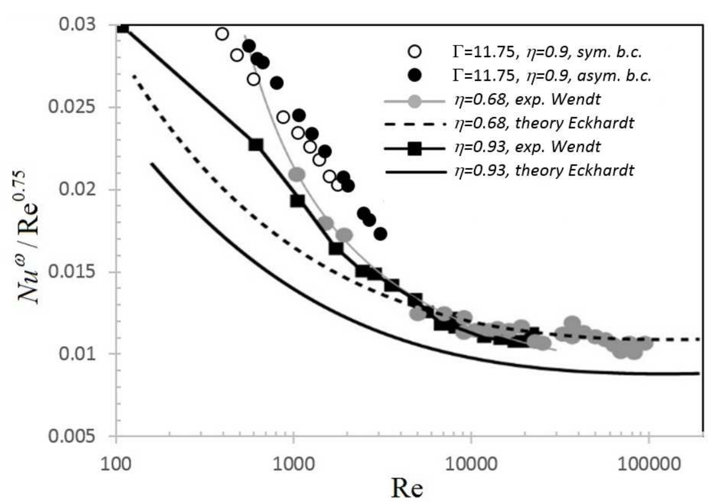

Fig. 10. The total current Nu^{ω} obtained in present paper in cavity of $\Gamma = 11.75$, $\eta = 0.9$ with the asymmetric and symmetric end-wall boundary conditions. Comparison with the experimental data obtained by Wendt [1] and with the theoretical results obtained by Eckhardt *et al.* [26], $\eta = 0.93$ and $\eta = 0.68$.

obtained by Lewis and Swinney [3]). In [14] the numerically obtained Nu^{ω} for co- and counter rotating cylinders was rescaled by $\mathrm{Re}_s^{0.76}$ (Re_s is the shear Reynolds number – for the stationary outer cylinder $\mathrm{Re}_s = 2\mathrm{Re}/(1+\eta)$). The exponent 0.76 was found for very large Re.

Eckhardt *et al.* [26] rescaled angular momentum current obtained theoretically for the flow case with the stationary outer cylinder $\mathrm{Nu}^{\omega}/\mathrm{Re}^{0.75}$ and presented it as a function of Re and η (Fig. 7 in [26]). The results obtained theoretically in [26] for $\eta = 0.68$ and 0.93 were compared to the experimental data of Wendt [1]. This analysis showed that for large Re the dependence of $\mathrm{Nu}^{\omega}/\mathrm{Re}^{0.75}$ on radii ratio η and on Re is vanishing. In the light of these data in Fig. 10 we analyze our results obtained for the asymmetric and symmetric end-wall boundary conditions. Due to the slight dependence of Nu^{ω} on radius (see Fig. 8) we introduce the averaged values. From Fig. 10 we can see that the present results are located above two lines obtained experimentally by Wendt [1] and above theoretical results obtained by Eckhardt *et al.* [26]. This can be attributed to the enhancement of the angular momentum transport caused by the end-wall boundary conditions. We also notice the slight difference between our results obtained for the asymmetric and symmetric end-wall boundary conditions.

5. Summary

In the paper the DNS/SVV results of the transitional Taylor–Couette flows have been presented. Investigations performed up to Reynolds number 3000 have allowed us to analyze all consecutive bifurcations appearing in the cavity of $\Gamma = 11.75$, $\eta = 0.9$ (with the rotating inner cylinder and bottom disk, and with the stationary outer cylinder and top disk). The DNS/SVV method based on Chebyshev and Fourier polynomials used in our investigations has proven to be an effective tool for solving the considered problem.

We have found that the radial profiles of the angular momentum (averaged in space and time) are almost constant in the central core. These constant values in the cores are in agreement with the experimental observations of Taylor [28] and Smith, Townsend [29] and numerical results of Brauckmann, Eckhardt [14]. We have also presented the radial profiles of the Reynolds stress tensor components averaged over cylindrical surfaces. The highest value is achieved by the azimuthal component $\langle\overline{v'v'}\rangle_{A(R)}$ with a maximum in the inner cylinder boundary layer. The profiles of the axial component $\langle\overline{w'w'}\rangle_{A(R)}$ also clearly demonstrate the existence of the boundary layers on both cylinders, but their values are smaller than the azimuthal ones. The radial component achieves maximum in the center of the cavity.

The presented snapshots of the velocity field show that there are two types of vortices: the large eddies generated by the instability mechanism connected with the curvature and small eddies resulting from the near-wall shear. The large scale structures retain their basic shape, despite the fact that they are surrounded by the small eddies. The snapshots show also vortices created in the bottom rotating disk boundary layer and in the top stationary one. In the Ekman boundary layer we observe nine vortices of the dimensionless wavelength $\lambda_a = 1.128$.

The statistical analysis of $\langle j^\omega \rangle_{\varphi,t}/J^\omega_{lam}$ have shown that the fluctuations in the middle sections are 20 times larger than the fluctuations at the inner and outer cylinders. The location of the local $\langle j^\omega \rangle_{\varphi,t}/J^\omega_{lam}$ extreme values are connected with the inflow and outflow jets. At the location of the outflow jets we observe the local maximum values of $\langle j^\omega \rangle_{\varphi,t}/J^\omega_{lam}$ at the outer cylinder and in the middle section, and the minimum at the inner cylinder. At the location of the inflow jets we observe the local minimum values at the outer cylinder and in the middle section, and the maximum values at the inner cylinder. The radial profiles of the total current normalized by its laminar value Nu^ω show slight dependences on the radius which is attributed to the influence of the end-wall boundary conditions. We observe this dependence for the symmetric and asymmetric end-wall boundary conditions. The rescaled angular momentum currents $\mathrm{Nu}^\omega/\mathrm{Re}^{0.75}$ obtained for different Reynolds numbers are compared with the experimental results of [1] and theoretical results of [26] ($\eta = 0.93$ and $\eta = 0.68$). The obtained results are slightly larger than these published in [1, 26], which can be attributed to the enhancement of the angular momentum transport caused by the end-wall boundary conditions. The study also shows that it would be of great interest to perform wider comparisons between experiments and simulations for the flow at moderate Reynolds numbers ($\mathrm{Re} < 3000$), where the largest influence of radii ratio on the Nu^ω distributions is observed.

6. Acknowledgement

The authors are grateful to the Poznań Supercomputing and Networking Center, where the computations have been performed.

References

1. F. Wendt, *Turbulente Strömungen zwischen zwei rotierenden konaxialen Zylindern*, Ing.-Arch., **4**, 577–595, 1933.
2. D.P. Lathrop, J. Fineberg, H.L. Swinney, *Turbulent flow between concentric rotating cylinders at large Reynolds number*, Phys. Rev. Lett., **68**, 1515–1518, 1992.
3. G.S. Lewis, H.L. Swinney, *Velocity structure functions, scaling, and transitions in high-Reynolds-number Couette–Taylor flow*, Phys. Rev. E, **59**, 5457–5467, 1999.

4. A. Racina, M. Kind, *Specific power input and local micromixing times in turbulent Taylor–Couette flow*, Exp. Fluids, **41**, 513–522, 2006.

5. A. Barcilon, J. Brindley, M. Lessen, F.R. Mobbs, *Marginal instability in Taylor–Couette flows at a high Taylor number*, J. Fluid Mech., **94**, 453–463, 1979.

6. B. Dubrulle, O. Dauchot, F. Daviaud, P.Y. Longaretti, D. Richard, J.P. Zahn, *Stability and turbulent transport in Taylor–Couette flow from analysis of experimental data*, Phys. Fluids, **17**, 095103, 2005.

7. A.K. Mujumdar, D.B. Spalding, *Numerical computation of Taylor vortices*, J. Fluid Mech., **81**, 295–304, 1977.

8. K.A. Cliffe, T. Mullin, *A numerical and experimental study of anomalous modes in the Taylor experiment,* J. Fluid Mech., **153**, 243–258, 1985.

9. O. Czarny, E. Serre, P. Bontoux, R.M. Lueptow, *Interaction of wavy cylindrical Couette flow with endwalls*, Phys. Fluids, **16**, 1140–1148, 2004.

10. K.T. Coughlin, P.S. Marcus, *Modulated waves in Taylor–Couette flow Part 1. Analysis*, J. Fluid Mech., **234**, 1–18, 1992.

11. K.T. Coughlin, P.S. Marcus, *Modulated waves in Taylor–Couette flow Part 2. Numerical simulation*, J. Fluid Mech., **234**, 19–46, 1992.

12. J.A. Vastano, R.D. Moser, *Short-time Lyapunov exponent analysis and the transition to chaos in Taylor–Couette flow*, J. Fluid Mech., **233**, 83–118, 1991.

13. S. Dong, *Direct numerical simulation of turbulent Taylor–Couette flow*, J. Fluid Mech., **587**, 373, 2007.

14. H. Brauckmann, B. Eckhardt, *Direct numerical simulations of local and global torque in Taylor–Couette flow up to Re D 30000*, J. Fluid Mech., **718**, 398, 2013.

15. T. Mullin, C. Blohm, *Bifurcation phenomena in a Taylor–Couette flow with asymmetric boundary conditions*, Phys. Fluids, **13**, 136, 2001.

16. K.A. Cliffe, T. Mullin, D. Schaeffer, *The onset of steady vortices in Taylor–Couette flow: The role of approximate symmetry*, Phys. of Fluids, **24**, 064102, 2012.

17. J. Abshagen, K.A. Cliffe, J. Langenberg, T. Mullin, G. Pfister, S.J. Tavener, *Taylor–Couette flow with independently rotating end plates,* Theoret. Comput. Fluid Dynamics, **18**, 129–136, 2004.

18. M. Avila, *Stability and angular-momentum transport of fluid flows between corotating cylinders,* Phys. Rev. Lett., **108,** 124501, 2012.

19. E. Serre, J.P. Pulicani, *A three dimensional pseudo-spectral method for convection in rotating cylinder*, J. Computers Fluids, **30**, 491, 2001.

20. E. Tuliszka-Sznitko, K. Kiełczewski, *Numerical investigations of Taylor–Couette flow using DNS/SVV method,* Comp. Method in Science and Tech., **21**, 211–219, 2015.

21. I.E. Tadmor, *Convergence of spectral methods for nonlinear conservation laws*, SIAM, J. Numerical Analysis, 26, **30**, 1989.

22. E. Severac, E. Serre, *A spectral viscosity LES for the simulation of turbulent flows within rotating cavities*, J. Comp. Phys., **226**, 2, 1234, 2007.

23. K. Kiełczewski, E. Tuliszka-Sznitko, *Numerical study of the flow structure and heat transfer in rotating cavity with and without jet,* Arch. Mech., **65**, 527, 2013.

24. J. Jeong, F. Hussain, *On the identification of a vortex*, J. Fluid Mech., **285**, 69, 1995.

25. P. Chakraborty, S. Balachandar, R.J. Adrian, *On the relationships between local vortex identification schemes*, J. Fluid Mech., **535**, 189–214, 2005.

26. B. Eckhardt, S. Grossmann, D. Lohse, *Torque scaling in turbulent Taylor–Couette flow between independently rotating cylinders*, J. Fluid Mech., **581**, 221–250, 2007.

27. D. Pirro, M. Quadrio, *Direct numerical simulation of turbulent Taylor–Couette flow*, European J. of Mechanics, B/Fluids, 27, 552–566, 2008.

28. G.I. Taylor, *Fluid friction between rotating cylinders, 1-torque measurements*, Proc. Roy. Soc., Ser. A **157**, 546, 1936.

29. G.P. Smith, A.A. Townsend, *Turbulent Couette flow between concentric cylinders at large Reynolds number*, J. Fluid Mech., **123**, 187–217, 1982.

30. B. Eckhardt, S. Grossmann, D. Lohse, *Scaling of global momentum transport in Taylor–Couette and pipe flow*, Eur. Phys. J. B **18**, 541–544, 2000.

Received February 28, 2016; revised version September 20, 2016.